Received: 24 November 2020 | Revised: 29 March 2021 | Accepted: 30 March 2021

DOI: 10.1002/esp.5129

RESEARCH ARTICLE

ESPL WILEY

Spatio-temporal assessment of the hydrological drivers of an active deep-seated gravitational slope deformation: The Vögelsberg landslide in Tyrol (Austria)

Jan Pfeiffer[1,2] | Thomas Zieher[1,2] | Jan Schmieder[1,2] | Martin Rutzinger[1,2] | Ulrich Strasser[2]

[1]Institute for Interdisciplinary Mountain Research, Austrian Academy of Sciences, Innsbruck, Austria

[2]Department of Geography, University of Innsbruck, Innsbruck, Austria

Correspondence
Jan Pfeiffer, Institute for Interdisciplinary Mountain Research, Austrian Academy of Sciences, Technikerstr. 21a, 6020 Innsbruck, Austria.
Email: jan.pfeiffer@oeaw.ac.at

Summary

Spatio-temporal variations of precipitation are presumed to influence the displacement rate of slow-moving deep-seated landslides by controlling groundwater recharge, pore-water pressure and shear strength. Phases of landslide acceleration responding to long-lasting rainfall and snowmelt events occur under site- and event-specific time delays. Assessing groundwater recharge and simultaneous recording of landslide displacement in a sufficient spatial and temporal resolution is essential to deepen the understanding of mechanisms controlling a landslide's deformation behaviour and is indispensable when it comes to identifying and developing target-oriented mitigation strategies. The objective of this study was to assess hydrological landslide drivers (solid and liquid precipitation, snowmelt and evapotranspiration) and to investigate their spatio-temporal distribution in the context of movements recorded at the Vögelsberg landslide (Tyrol, Austria). Hydrometeorological variables were simulated using the AMUNDSEN (Alpine MUltiscale Numerical Distributed Simulation ENgine) hydroclimatological model and landslide movements were continuously monitored using an automated tracking total station. Area-wide simulated time series of available water were used: (i) to separate them into single landslide triggering hydrometeorological events; (ii) to analyse spatio-temporal patterns of water availability per triggering event including individual response times; (iii) to delineate an effective hydrological landslide catchment; and (iv) to identify relations between assessed water input and landslide displacement rate. For the observation period from 05-2016 until 06-2019 we identified three distinctive hydrometeorological events causing time-delayed periods of landslide acceleration. Spatio-temporal differences in water availability per triggering event result in spatially diverse response times varying from 20 to 60 days for rainfall-triggered events and between 0 and 8 days for events triggered by snowmelt. Pronounced spatio-temporal differences of snowmelt within the model domain were identified to offer a unique possibility to delineate the effective hydrological landslide catchment. While considering event-specific time-lags, logarithmic correlations between incoming water and landslide displacement rate become apparent.

KEYWORDS
AMUNDSEN, automated tracking total station, hydrological modelling, landslide displacement, OPERANDUM, time series analysis

1 | INTRODUCTION

Large mass movements such as deep-seated gravitational slope deformations (DSGSDs) are common phenomena in mountain ranges across the world, affecting entire mountain slopes from the valley bottom to the slope's ridge (Agliardi et al., 2012; Crosta et al., 2013). They are typically complex and large systems of slope failures characterized by tensional morphological features in the upper part and compressional features in the lower part. These features originate from long-term displacements of a few millimetres per year, as it was identified to be common for DSGSD (Ambrosi & Crosta, 2006; Varnes et al., 1990; Zangerl et al., 2010). In several cases DSGSDs are accompanied by secondary, more active subunits preferentially occurring on highly fractured and intensely deformed rock masses on the bulged toe of the DSGSD (Bovis & Evans, 1996; Crosta et al., 2014). Such landslide subunits can show enhanced, fluctuating displacement rates ranging from centimetres to several metres per year (Brückl et al., 2013; Pfeiffer et al., 2018; Zieher et al., 2019). In some cases they accelerate and result in catastrophic slope failures such as rockslides and rock avalanches, endangering human well-being and infrastructure situated on the top of the landslide or within its potential run-out area (Carlà et al., 2017; Ostermann & Sanders, 2017).

Changing landslide displacement rates over time are commonly associated with fluctuating pore-water pressures subject to spatio-temporally varying rainfall and snowmelt, permitting groundwater recharge. Infiltrating precipitation reduces the shear strength by increasing the pore-water pressure when reaching the landslide's governing aquifer. The pore-water pressure-controlled reduction of the effective normal stress can then lead to increased slope movement rates (Terzaghi, 1950). Several studies investigating the relations between precipitation and landslide displacement rate have been carried out. (Iverson & Major, 1987; Lacroix et al., 2020; Van Genuchten & Van Asch, 1988). Handwerger et al., (2013), for example, investigated the controls on seasonal deformation of multiple slowly moving landslides using satellite radar interferometry (InSAR) and precipitation data recorded at a rain gauge approximately 30 km away from the landslide area. Bievre et al. (2018) combined extensive geophysical, geotechnical and hydrogeological investigations towards a better understanding of the causes of seasonal variations of displacement rates. They used cross-correlations between hydrometeorological and piezometer time series to prove a preferential water infiltration path in a slow-moving clayey earthslide. Macfarlane (2009) used geodetic surveys combined with extensometers, inclinometers, piezometers, flow-measuring weirs and records of a nearby rain gauge to investigate and further predict the behaviour of large, slowly moving landslides in reservoir settings. Brückl et al. (2013) presented an integrated monitoring approach combining geodetic, hydrological and seismological methods to assess the displacement over time and its potential drivers. The authors paid particular attention to the influence of snowmelt, which was assessed on site by weekly snow water equivalent measurements at points along a slope profile. Together with liquid precipitation recorded at a nearby weather station, they estimated infiltration as a proxy for the hydrostatic water level to support early warning. Similar investigations are described in Crosta et al. (2014), where snowmelt was identified to be a major cause in the context of landslide acceleration. Osawa et al. (2018) carried out detailed investigations to retrieve a comprehensive understanding of hydrological processes (i.e., snowmelt and rainfall) in the context of a slow-moving landslide. Additional effects of evapotranspiration were accounted in the study by Coe (2012), where a regional moisture balance index was retrieved to analyse future landslide movements considering climate change projections.

Most of these studies depict the existence of manifold methods to assess landslide movements. Continuous or periodic measurements estimating displacements on or below the surface in an area-wide or at an individual point scale find application in a target-oriented measurement setup. But when it comes to the assessment of the hydrological input, most of these studies rely on precipitation records measured at single points with conventional gauge systems, either neglecting spatial differences in precipitation or neglecting the time-delayed effect of melt water being released from the snow pack after the winter season. Investigating hydrological drivers of deep-seated landslides in a large DSGSD setting demands continuous and precise information of landslide displacement together with a temporally and spatially highly resolved product of water available for groundwater recharge. Where a large variety of methods for estimating landslide displacements in either high temporal or spatial resolution are applied in several case studies, the on-site acquisition of precipitation, evapotranspiration and snowmelt is not practicable in high temporal and spatial resolution (Brückl et al., 2013).

Physically based hydroclimatological models driven with atmospheric variables recorded at well-distributed surrounding weather stations overcome this issue and allow a practicable assessment of available water in high temporal but also high spatial resolution. They provide unique information about rainfall and snowfall, including the temporary storage of snow and the delayed release of snowmelt water, which leads to very pronounced spatio-temporal differences in the availability of water in Alpine regions. These models are frequently applied in glaciological and hydrological investigations focusing on the assessment of current and future water resources in mountainous regions (Hanzer et al., 2016; Marke et al., 2015; Strasser, 2008). Furthermore, their ability to simulate potential groundwater recharge time series for every raster cell within a catchment emphasizes their importance in investigating the spatio-temporal distribution of hydrological landslide drivers. Although modelling-based approaches aiming to assess landslides influencing water availability were presented in the past, they demonstrate a lack in spatial completeness or model complexity considering the physical processes determining snowpack evolution (de Palézieux & Loew, 2019; Vallet et al., 2015).

No study so far has aimed at analysing the different spatio-temporal characteristics of available water forcing groundwater recharge associated with landslide acceleration, which is assumed to offer a novel way for creating a deeper understanding of hydrological drivers of landslides. Having a spatially distributed product of water availability in a sufficient temporal resolution derived from a physically based hydroclimatological model is supposed to create several advantages and possibilities important for identifying mitigation measures when comparing them with landslide movement records. The benefits of an area-wide product compared to non-area wide products are manifold. Among them, the mapped distribution of water availability per landslide-triggering event can help to indicate areas of higher water avilability. Performed raster cell- and event-wise comparative analysis of water input and landslide displacement time series can be used to estimate an event-specific time lag between hydrological

input and landslide acceleration. This time lag, further defined as the landslide response time and assessed for every raster cell, forms maps of response times valid for each identified triggering hydrometeorological event. These maps support the delineation of the landslide's effective hydrological catchment by excluding areas where water availability cannot be responsible in forcing a landslide's acceleration (e.g., when the moment of water availability occurs after the landslide acceleration). Estimated event-specific time lags are further necessary to derive models allowing the prediction of landslide movements as a response to hydrological input. Retrieved outcomes help in understanding the landslide triggers and are therefore beneficiary in planning and locating target-oriented measures aiming to reduce a landslide's displacement rate (Bonzanigo et al., 2007; Eberhardt et al., 2007).

In this study the hydrometeorological drivers forcing movements of the Vögelsberg deep-seated landslide were assessed and analysed in a spatio-temporal way by using the hydroclimatological model AMUNDSEN (Alpine MUltiscale Numerical Distributed Simulation ENgine) (Strasser, 2008). While paying special attention to the more complex simulation of the snow cover evolution, simulated snow depths and snow masses were validated in detail to provide an accurate information of snowmelt, which forms the water availability together with rainfall and respecting the withdrawing effect of evapotranspiration. Hydrometeorological events responsible for phases of landslide acceleration were temporally delimited using a rule-based segmentation approach and examined considering their spatial characteristics. Area-wide cross-correlations between statistics of hydrometeorological time series and monitored landslide displacement rate were derived and investigated on an event basis to derive individual landslide response times for every raster cell within the catchment. By only considering non-negative response times, an effective hydrological landslide catchment was delineated and a time series of thereon aggregated water availability was used for detailed analysis of interactions between landslide-controlling hydrometeorological processes and displacement rates.

The objectives of the present study were:

- to assess hydrological drivers controlling landslide displacement using a hydroclimatological model;
- to extract hydrometeorological events causing pronounced landslide accelerations including individual response times;
- to delineate the effective hydrological landslide catchment; and
- to identify and analyse the temporal and spatial correlations of hydrometeorological events and related increase in landslide displacement rate.

2 | STUDY AREA

The Vögelsberg DSGSD is situated on a northeast-facing slope at the lower Watten valley in Tyrol, Austria (Figure 1). The DSGSD system covers an area of approximately 4.6 km^2 and ranges from 750 m above sea level (a.s.l.) at the valley bottom to the double-crested mountain ridge at elevations of 1200 m a.s.l. in the north and 2200 m a.s.l. in the south. A currently active and slowly moving part (approx. 0.2 km^2 (see black polygon in Figure 1b) embedded in the lower section of the DSGSD shows temporally varying displacement rates, causing serious damage to infrastructure and houses. In a long-term perspective, continuous movements in the range of several centimetres per year cause a steepening of the foot slope, bearing the risk of sudden slope failures, potentially damming the underlying Watten River.

Lithologies favouring prevailing slope deformation processes belong to the Innsbrucker Quartzphyllite complex of the central Eastern Alps (Rockenschaub et al., 2003). Sericite phyllites, chlorite-sericite phyllites and quartz phyllites with intercalated calcareous marbles are apparent at the investigated slope. Greenschist (prasinites) are exposed around the summit of the Largoz, which is the highest point in the DSGSD catchment (red polygon in Figure 1a, b). Core drillings on the actively creeping slab record a shallow quaternary cover above strongly disintegrated quartz phyllite fragments dominated by clay, silt, sand and gravel grain sizes up to depths of 52–70 m below the surface indicating a long and intense history of deformation. This sequence of unconsolidated rock is further assumed to represent the landslide depth where inclinometer measurements indicate distinct displacements between 43 and 51 m below the surface (Engl, 2018).

Dispersed settlements and pastures speckled by some smaller forested areas characterize the catchment between 750 and 1200 m a.s.l. Above 1200 m a.s.l. a uniform spruce forest (*Picea abies*) dominates the land cover. The highest areas in the catchment (1800–2200 m a.s.l.) are characterized by natural grassland scattered by single Swiss stone pine trees (*Pinus cembra*). The map in Figure 1b shows the the land cover types occurring in the study area. The close-by weather station 'Rinn' (960 m a.s.l.), located approximately 8 km to the east of the active landslide, records a mean annual precipitation of 896 mm between 2008 and 2018, of which 13% is snowfall, considering a temperature threshold of 1°C. Even larger amounts of snowfall are assumed to accumulate at high elevations in the catchment, with great potential to recharge groundwater during spring and early summer snowmelt periods, whose precise quantification is part of this study. The study area represents a case study investigated within the scope of the OPERANDUM project aiming to investigate nature-based solutions for hydrometeorological risk reduction (Ruangpan et al., 2020).

3 | MATERIALS AND METHODS

3.1 | Monitoring the landslide movement

The slope's movement is monitored by an automated tracking total station (ATTS) operated by the the Department of Geoinformation (Federal State of Tyrol), measuring the position of 48 artificially installed retroreflecting prisms. The ATTS performs hourly distance measurements and has been in operation since May 2016. Nineteen targets show displacements clearly above the measurement accuracy of ±0.54 cm/a (standard deviation of the decomposed time series). They indicate the extent of the more active landslide part. Recorded displacements at the other 29 prisms are below the assumed measurement accuracy and further assumed as stable. Targets are mounted either on buildings or artificially installed piles. The hourly measurements were aggregated to daily mean coordinates, which

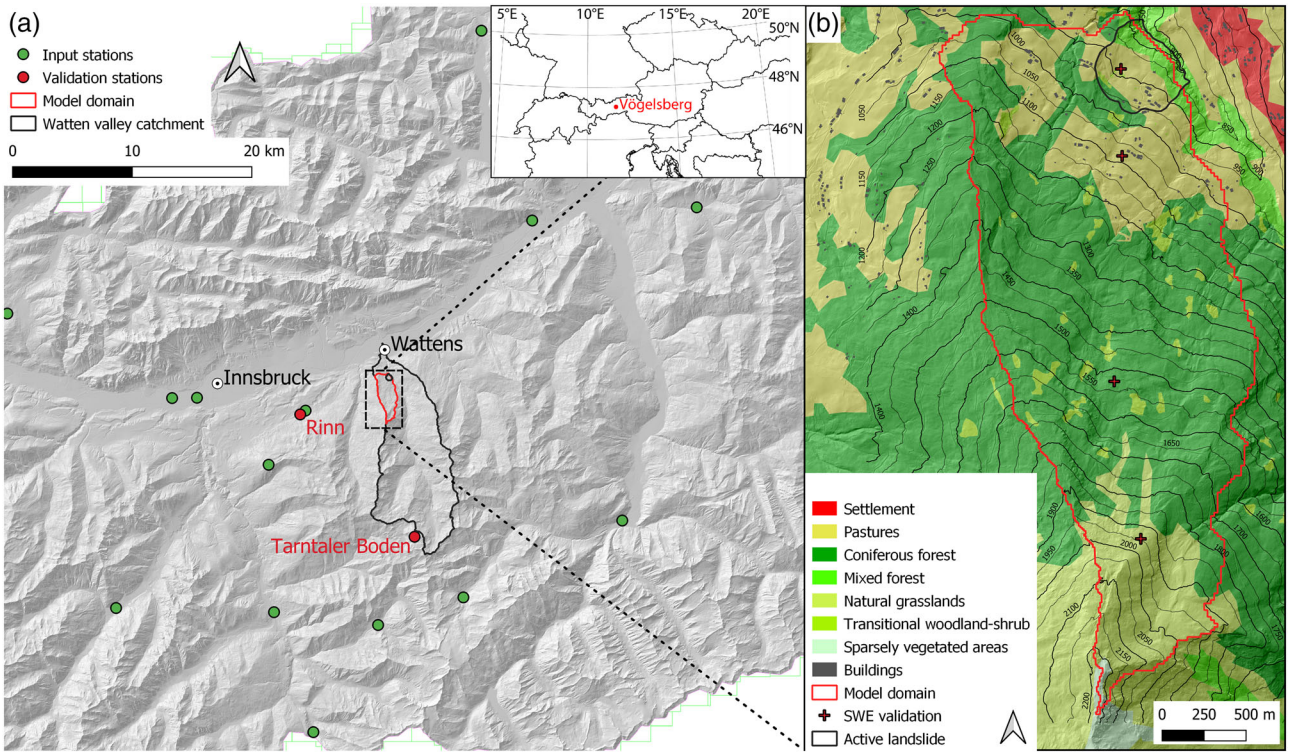

FIGURE 1 (a) Spatial distribution of weather stations used for hydroclimatological modelling and validation around the study area. (b) Adapted CORINE land cover types in the model domain

were used to estimate cumulative displacements and displacement rates. Time series of displacement rates were further smoothed using a moving average within a considered window of 20 days. This window size turned out to be a suitable time span in which the effect of outliers could be minimized by still considering accurate temporal information of changes in displacement rate. For further analysis and correlation with hydrological time series, mean displacement rates were calculated based on the 13 prisms distributed on the active landslide part, which cover the same observation period.

3.2 | Modelling the water input

3.2.1 | Model description, setup and input data

Rainfall and snowmelt are the main water input sources within the catchment of the DSGSD analysed in this study, and their spatio-temporal variability is essential for the quantification of the relevant hydrological drivers. But quantifying time-varying distributed water input is not feasible by point measurements of precipitation, for example, due to the spatial variability or the temporary storage in the snow cover and the delayed release during snowmelt. Therefore, we used the hydroclimatological model AMUNDSEN to simulate the water input potentially available for infiltration (i.e., rainfall and snowmelt minus evapotranspiration) at the catchment scale. AMUNDSEN is a modular fully distributed hydroclimatological model (Strasser, 2008) designed to simulate the evolution of mountain snow cover (i.e., the accumulation and ablation) and has been validated at diverse Alpine sites with complex terrain (Hanzer et al., 2016; Marke et al., 2015; Pellicciotti et al., 2005; Strasser et al., 2008).

Model features are precisely described in Strasser (2008). Here, the aspects relevant to the model setup used in this study are pinpointed. Point measurements of meteorological variables (T_a: air temperature; P: precipitation; RH: relative humidity; WS: wind speed; G: global radiation), a digital elevation model, a soil map and a land cover map of the model domain are used as input for AMUNDSEN. Measurements of meteorological variables (T_a, P, RH, WS, G) were obtained from 13 stations of the national weather service of Austria 'Zentralanstalt für Meteorologie und Geodynamik' (ZAMG), hereafter called ZAMG stations. The ZAMG stations cover an elevation range of 530–2247 m a.s.l. and are located within a radius of approximately 30 km of the Vögelsberg DSGSD (Figure 1a). The digital elevation model provided by the Federal state of Tyrol (Division of Geoinformation) was aggregated to 20 m grid cells. Landcover information was derived from the CORINE (Coordination of Information on the Environment) 2018 dataset and refined using an orthophoto from 2019 to consider recent forest clearings. Data from the European Soil Database was used as soil map input (European Commission and the European Soil Bureau Network, CD-ROM, EUR 19945 EN, 2004).

Interpolated fields of the measured meteorological variables (T_a, P, RH, WS) were derived by a combined lapse rate–inverse distance weighting scheme using calculated lapse rates at each time step. G was interpolated accounting for topographic effects. The type of precipitation was determined by the wet bulb temperature threshold ($T_w = 0°C$) and the energy balance approach was used to simulate the snow cover evolution. Submodules 'canopy' and 'evapotranspiration' were enabled because of the high forest cover (66% in the model domain) and to subtract evapotranspiration from rainfall as potential water input during the snow-free period.

We ran AMUNDSEN with a temporal and spatial resolution of 3 h and 20 m (grid cell size), respectively. To ensure a spatial comprehensive assessment of the landslide's hydrological drivers, a model domain representing the whole above area of the lowest point of the active landslide was delimited. This was done by applying an algorithm for estimating flow directions and upslope areas proposed by Tarboton (1997) to a sink-filled and 20 m resampled digital terrain model derived from airborne laser scanning data acquired in 2007. This generously defined area was chosen to be the AMUNDSEN model domain in which the area-wide water input should be simulated and analysed regarding associated slope movements (see red polygon in Figure 1). AMUNDSEN was applied for the period 1 October 2006 to 30 June 2019. Grids of daily rainfall, snowmelt and evapotranspiration sums were aggregated and used for further landslide interpreting analyses (Figure 2). Further model outputs used for validation (snow depth, snow water equivalent) are described in Section 3.2.2.

3.2.2 | Model validation

Snow depth time series of two weather stations ('Rinn', 'Tarntaler Boden'; Figure 1a) were used to validate the AMUNDSEN model results for the period 1 October 2015 to 30 June 2019, in accordance with the period of available ATTS measurements. Snow depth at the ZAMG station 'Rinn' (924 m a.s.l.) is measured daily at 07:00 (local time) and snow depth at the weather station 'Tarntaler Boden' (2544 m a.s.l.) of the Austrian Research Centre for Forests is measured automatically at 10 min intervals and was aggregated to the modelling time step (3 h). The stations represent the lower and upper elevation bound to capture almost the complete elevation range of the study area. Comparing these weather station records with the AMUNDSEN simulated snow depth time series at the respective station locations indicates the quality of the model. In situ snow water equivalent (SWE) measurements carried out on five dates during winter 2019 at four different locations (Figure 1b) were used to additionally assess the quality of the AMUNDSEN snow mass simulations.

The spatial extent of the snow cover was validated with the Theia Snow collection, a high-resolution product derived from Sentinel-2 scenes (Gascoin et al., 2019), for the years 2017, 2018 and 2019. This product offers snow cover information since late 2017 at the same spatial resolution as the AMUNDSEN grids (20 m). Sixty-eight scenes were preselected according to a maximum cloud cover of 10% in the model domain. Forested areas were excluded for validating the snow extent because a detection of snow below the canopy is not accomplishable based on optical imagery. This resulted in an area of 1.4 km^2 for validating the spatial extent of simulated snow cover. AMUNDSEN snow cover maps were derived from snow depth fields closest to the time of the satellite passing, considering a snow depth threshold of 2 cm, as suggested by Gascoin et al. (2019).

The following goodness-of-fit criteria were chosen to measure the fit of the AMUNDSEN modelling results. The Kling–Gupta efficiency (KGE Kling et al., 2012), the coefficient of determination (R^2) and percent bias (PBIAS) were used for validating the simulated snow depth time series and plot-scale SWE values. KGE values vary in the range of $-\infty$ to 1, and R^2between -1 and 1, where respective optima between simulated and observed values are 1. The optimal value of PBIAS, on the other hand, is 0, where positive values indicate overestimation and negative values indicate underestimation. The critical

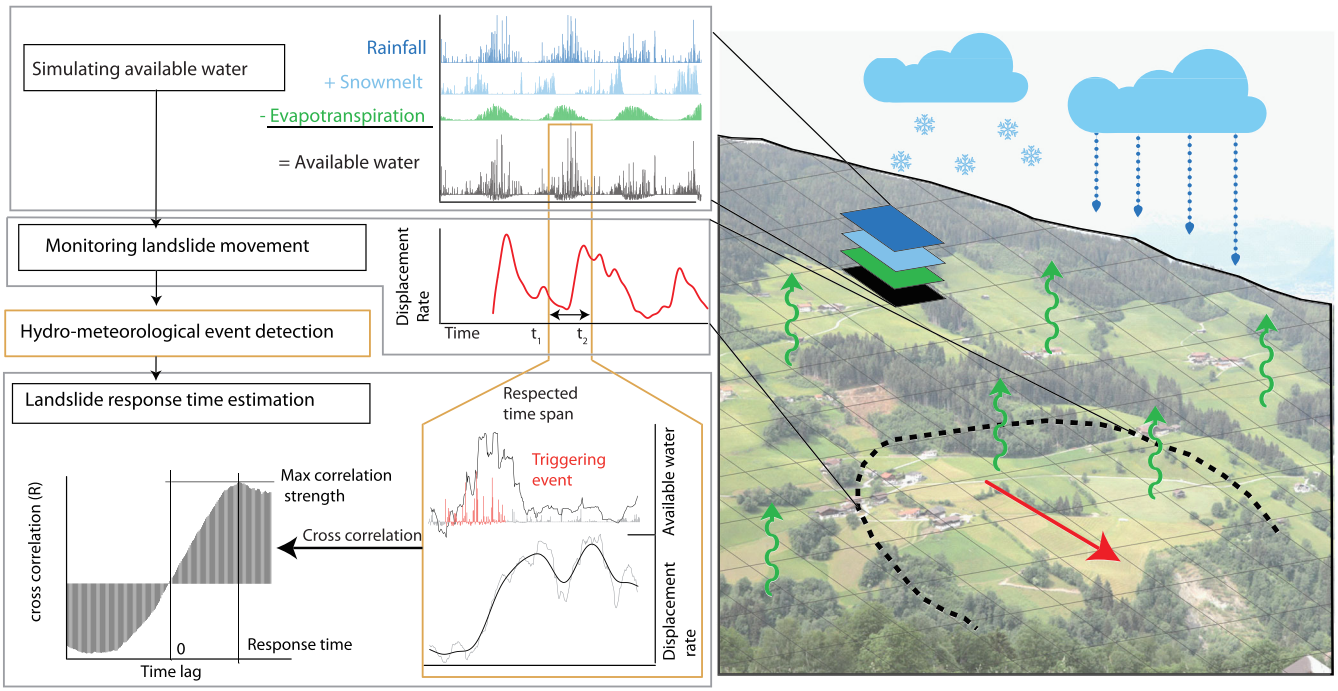

FIGURE 2 Illustrative summary showing the workflow followed in this study. Time series of catchment-wide simulated available water and monitored landslide movement were used to assess landslide accelerating events and their respective response time. The right-hand picture indicates hydrological processes occurring on the Vögelsberg DSGSD and influencing the currently active and faster-moving part (dashed black line) photographed from the opposite slope of the Watten valley

success index (CSI; see Equation (1)) was chosen to measure the goodness of fit of the snow cover extent based on true positive (TP), false positive (FP) and false negative (FN) estimated raster cells:

$$\mathrm{CSI} = \frac{\mathrm{TP}}{\mathrm{TP} + \mathrm{FP} + \mathrm{FN}}. \quad (1)$$

The CSI is a sensitive contingency table-based criterion to compare observed and simulated snow cover pattern in each raster cell. Additionally, the overall accuracy (ACC) and BIAS were used as comparable criteria to assess the quality of simulated and observed snow cover. ACC is defined as the number of correct simulations divided by the number of samples. The BIAS is defined as the frequency of correct snow cover simulations divided by the number of times where snow cover is observed. All three goodness-of-fit criteria approach a perfect score with a value of 1 (Hanzer et al., 2016; Zappa, 2008).

3.3 | Hydrometeorological event detection

Hydrometeorological events define time spans of increased water availability for infiltration and groundwater recharge. Intensity and duration of prolonged rainfalls were identified to be important parameters controlling the evolution of shallow landslides (Caine, 1980; Guzzetti et al., 2008). Assuming that hydrometeorological events with a critical intensity duration relation also trigger acceleration phases of more complex, slow-moving and delayed responding deep-seated landslides, an approach for estimating their thresholds was deployed. Time series of modelled rainfall, snowmelt and evapotranspiration were consolidated to a common time series of water potentially available for infiltration while neglecting the unknown portion of surface runoff. A segmentation approach, as successfully applied in (Meißl et al., 2020) to investigate runoff response to rainfall events, was modified and tailored to site- and process-specific conditions of the Vögelsberg DSGSD.

The event separation in Meißl et al. (2020) is done by passing through a time series of rainfall measurements at 15 min resolution and assigning events when fulfilling certain predefined conditions such as exceeding a detection limit and a minimum duration while adhering to a maximum pause and a minimum sum of rainfall within the event. Instead of using rainfall measurements recorded at gauges in a sub-day resolution, we used a spatially aggregated time series of the running sum of daily available water simulated with AMUNDSEN (see Section 3.2) to extract respective events. A 10-day window for calculating the running sum of available water performed best in indicating time spans of increased water availability matching with subsequent phases of increased landslide displacement rate. While passing through the time series, only values exceeding a duration of 5 days and a minimum sum of 50 mm of the 10-day running sum of available water were considered to form an event. Single events were separated if the running sum of available water dropped below 5 mm for at least 4 days.

This setting of parameters allows a reasonable extraction of hydrometeorological events under the scope of identifying the hydrological trigger of a sluggish responding landslide acceleration. Identified hydrometeorological events are assigned as landslide-triggering events if they can be associated with subsequent and significant increase of landslide displacement rate. Respective event statistics such as duration, total available water and associated change in landslide displacement rate can be extracted for each event. Knowing the approximate time span of each triggering event is an essential requirement for further landslide response time estimations (Figure 2).

3.4 | Event-based response time estimation

Landslide response to long-lasting rainfall or snowmelt varies considering event- or site-specific hydraulic characteristics. Knowing the landslide response times can be beneficial in estimating the landslide's characterizing hydraulic properties. Time series of water input and landslide displacement rates offer essential information for estimating event-specific landslide response times, which is assumed to represent the minimum time necessary for sufficient pore pressure changes in the landslide's governing aquifer to trigger its acceleration. In general, a slow landslide response would either indicate a low hydraulic permeability of the involved aquifer or great distances between infiltration zone and landslide. On the other hand, a quick landslide response would indicate high hydraulic permeability or infiltration occurring close to the active landslide part.

We used the area-wide simulated time series of water availability to assess response times for every raster cell in the predefined model domain. Assuming different response behaviours referring to different event characteristics, additional knowledge of the temporal boundaries of triggering events was considered for a catchment-wide response time estimation. We used a cross-correlation approach to estimate respective response times, as it is proven to be an appropriate way for an automated assessment of time lags between precipitation and landslide displacement rate time series of hydrologically driven landslides (Bievre et al., 2018; Lollino et al., 2002, 2006). The cross-correlation function (R_{xy}) describing the correlation between the function of available water (x_t) and landslide displacement rate (y_t) under varying time lags (τ) is expressed as

$$R_{xy}(\tau) = \sum_{t=-\infty}^{\infty} x_t y_{t+\tau}. \quad (2)$$

The occurrence of a maximum value within the respective cross-correlation function (R_{xy}) locates the time lag indicating the best conformity of hydrological and geodetic time series, which in our case is interpreted to be the landslide response time. We used prior identified event time spans extended by 6 months towards both sites and used them as thresholds to extract time series of available water to assure a complete input for the cross-correlation per triggering event (Figure 2). A time series of the running sum of the available water was cross-correlated with the mean displacement rate time series. To identify an appropriate proxy of available water with the best ability to predict the time-delayed course of the accelerating landslide displacement rate curve, different time windows for deriving the running sum were tested. Windows ranging from 2 to 150 days were considered to build the time series of the running sum. Each summed time series was cross-correlated with the mean displacement rate series, where the course of the correlation strength with varying window size was used as an indicator to determine an appropriate window size.

Computed cross-correlation functions between the identified best-fitting running sum time series of available water and mean displacement rate time series were used to identify the time delay of landslide acceleration potentially responding to prolonged hydrometeorological input by locating respective maximums therein (Figure 2). This time delay can be calculated for each prior identified landslide triggering event and every cell of the hydroclimatological model output. Using a time series of water availability aggregated to a landslide's effective hydrological catchment enables the estimation of an overall landslide response time. The described workflow was composed using the programming language R (R Core Team, 2020).

4 | RESULTS

4.1 | Landslide movement

Landslide displacement rates derived from repetitive ATTS measurements recording coordinates of the installed retroreflecting prisms moving on top of the landslide vary in magnitude but are consistent in terms of acceleration and deceleration periods, except for four targets, indicating a more constant movement in the order of 1.40 cm/a without pronounced fluctuations. These targets are located in the southeastern part of the active landslide body and indicate the existence of a subunit not being controlled by hydrometeorological variations. For further analysis these records of movement were neglected since the focus of this study was to investigate causes of varying movements in time as a response of hydrological input. Figure 3 shows the displacement rates and position of the 13 targets used for landslide movement interpretation. These targets cover the same observation period; hence their mean displacement rate (black line in Figure 3a) was used for further analysis and interpretation hereafter.

Within the respected time span three major phases of increased landslide displacement rate can be identified. The temporal occurrence of these phases does not show a periodicity or seasonality. The most pronounced acceleration occurred right after implementing the ATTS monitoring, where its start has not been fully recorded. Maximum displacement rates of 5.71 cm per year were recorded at mid-August 2016. A subsequent phase of deceleration was followed by a second acceleration phase starting in mid-July 2017 and reaching its maximum displacement rate of 4.98 cm per year in February 2018. A third landslide acceleration phase was recorded after another period of reduced movement. Maximum displacement rates of 3.57 cm per year were recorded in March and April 2019. Between deceleration and acceleration phases displacements of 1-2 cm per year prevail.

4.2 | Validation of the hydroclimatological model AMUNDSEN

The quality of simulated hydrometeorological time series was evaluated by paying particular attention to the more complex and challenging simulation of snow cover. We compared simulated spatio-temporal snow cover characteristics using the AMUNDSEN model with (i) respective snow depth time series measured at nearby weather stations, (ii) field measurements of snow water equivalent at selected locations and (iii) a satellite-based snow cover product.

The temporal pattern of snow cover evolution (e.g., ablation, accumulation and subsidence) throughout the winter matches very well with respective snow depths measured at the weather stations 'Rinn' and 'Tarntaler Boden' (Figure 4b,c). Only small differences in snow depth can be observed between simulated and measured snow depths. In general, the model underestimates measured snow depths. The onset of snowmelt and the date of snow cover depletion show a maximum time offset of −3 days compared to observations at the 'Tarntalerboden' and −9 days at the 'Rinn' weather station. Consequently, the snow cover vanishes only a few days earlier in the model than at the respective snow height validation stations. With the exception of these small offsets, the overall temporal pattern of decreasing snow depth during the melting season is represented well.

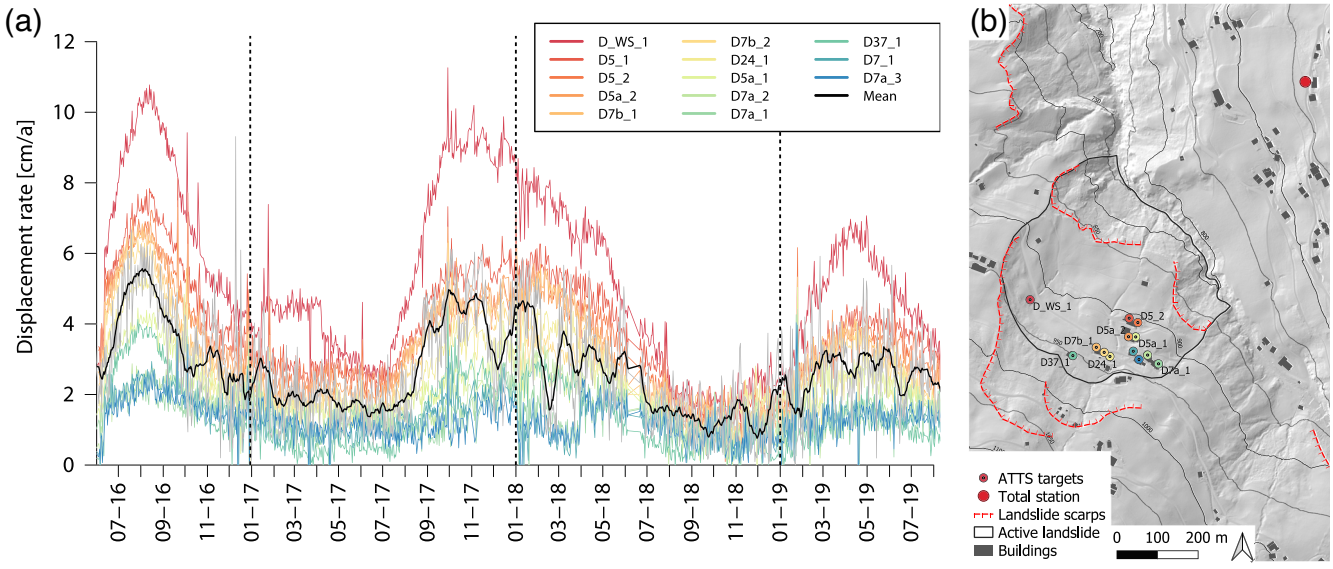

FIGURE 3 (a) Time series of averaged landslide displacement rates recorded at individual targets (coloured graphs) and mean displacement rate curve (black graph). Dashed vertical black lines indicate 1 January of respective year. (b) Overview of the active landslide and position of respective targets measuring its displacement

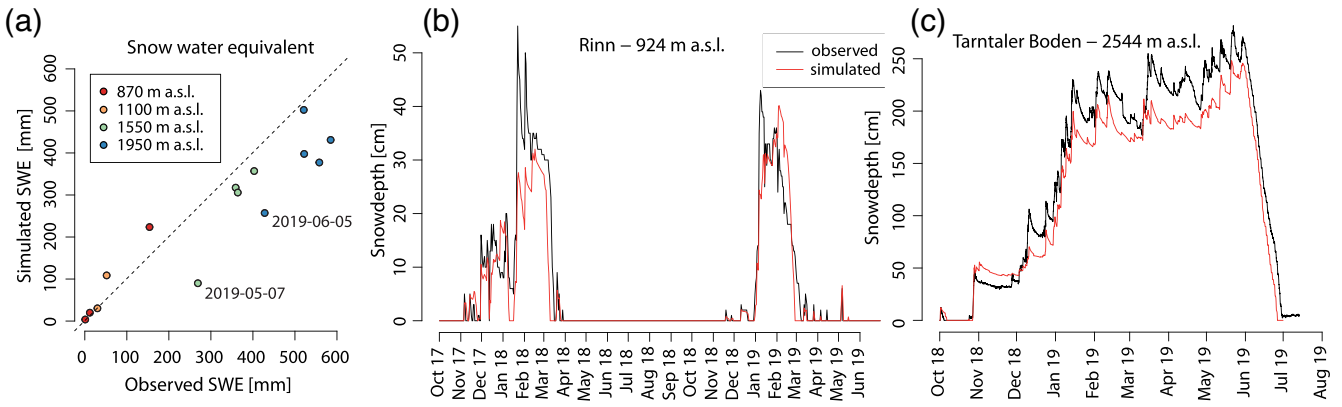

FIGURE 4 Point validation of simulated snow cover. Comparison between simulated and observed snow water equivalent (a) and snow depth time series: (b) Rinn station; (c) Tarntalerboden station). Location of respective validation position is shown in Figure 1

Simulated and observed snow water equivalent (SWE) values are generally in good agreement, indicating a robust model performance in simulating snow mass (Figure 4a). Only small overestimations at snow pit locations at lower elevations and underestimations at snow pits located at higher elevations are obvious but still in an acceptable range. Greater differences between simulated and observed snow mass preferentially occur towards the end of the ablation period. Nevertheless, calculated goodness-of-fit measures such as KGE, R^2 and PBIAS indicate a good performance of the AMUNDSEN model in simulating snow depth and snow mass throughout the winter (Table 1).

The spatio-temporal validation of the snow cover extent derived from simulated snow depth grids compared to snow cover maps based on Sentinel-2 imagery is shown in Figure 5. Only open land (land cover classes 'Pastures' and 'Natural grasslands'; see Figure 1b) has been considered for validation because in forested areas the snow cover extent cannot be derived from spaceborne optical imagery. The considered metrics, including the overall ACC, CSI and bias, generally indicate a good agreement between simulated results and the reference snow cover maps. The median of the overall ACC is 0.95, with slightly higher values in the lower areas compared to the areas at higher elevation. The same holds true for the CSI, which has a median value of 0.90. Spatial patterns of varying CSI values are mostly related to topography and influence of shadows in the vicinity of forests. The median bias is 1.07, indicating a minor overestimation of the simulated snow cover. The BIAS does not show a distinct variation in elevation. Overall, the validation indicates that the patterns of snow cover based on the simulation results are in agreement with the reference in both space and time.

4.3 | Hydrometeorological events

Hydrometeorological events were derived from the simulated time series of potentially infiltrating water considering simulated daily rainfall, snowmelt and evapotranspiration. In total, 22 events were detected over the period 2015-09-02 to 2019-06-14 using a time series of the 10-day running sum of available water averaged over the model domain. Three outstanding events considering their pronounced intensity and duration were identified to correlate with phases of landslide acceleration, since their temporal occurrence coincides with later recorded increase in landslide displacement rate

TABLE 1 Kling–Gupta efficiency (KGE), R^2 and percent bias (PBIAS), indicating quality of simulated snow fall depths and snow water equivalent against respective observed values

Station	KGE (–)	R^2 (–)	PBIAS (%)
Tarntaler Boden	0.81	0.98	−13.30
Rinn	0.76	0.84	−17.80
SWE field measurements	0.69	0.86	−19.60

(Figure 6). They lasted for 106, 132 and 209 days and implicate sums of 439, 471 and 609 mm of water potentially contributing to an increase of pore-water pressures in the active landslide body. Derived totals of event water are quite close to the simulated annual average of 643.5 mm of available water after subtracting evapotranspiration occurring in the period 2006-10-01 to 2018-09-30 in the model domain.

The composition in terms of involved origin of water differs between the identified landslide-triggering hydrometeorological events. We observed a primarily rainfall-dominated (event #2), a mainly snowmelt-dominated (event #3) and a combined (event #1) event. The smaller quantities of rainfall contained in event #3 are associated with rainfall that occurred after the landslide acceleration. Characteristics of these triggering events and a comparison to annual average values are summarized in Table 2. The greatest impact on landslide displacement rate is associated with event #1, where an accompanying increase of 3.81 cm/a of the mean landslide displacement rate was recorded. Even though events #3 and #2 are quite similar in terms of duration and amount of water availability, their coinciding increase in landslide displacement rate is different. Where the snowmelt-dominated event #3 causes a mean displacement rate increase of 1.75 cm/a, the rainfall-dominated event #2 causes an increase of 2.87 cm/a.

Besides event duration, magnitude, composition and associated increase in landslide displacement rate, additional spatial variations of simulated water availability are observable. Most pronounced spatial differences occur during events, where snowmelt contributes considerable amounts of available water within the model domain (Figure 7a,c). According to the model results, most of the water potentially contributing to groundwater recharge is available in the upper non-forested catchment areas (e.g., elevations above 1500 m a.s.l.). But also non-forested areas at lower elevations (1000–1200 m a.s.l.)

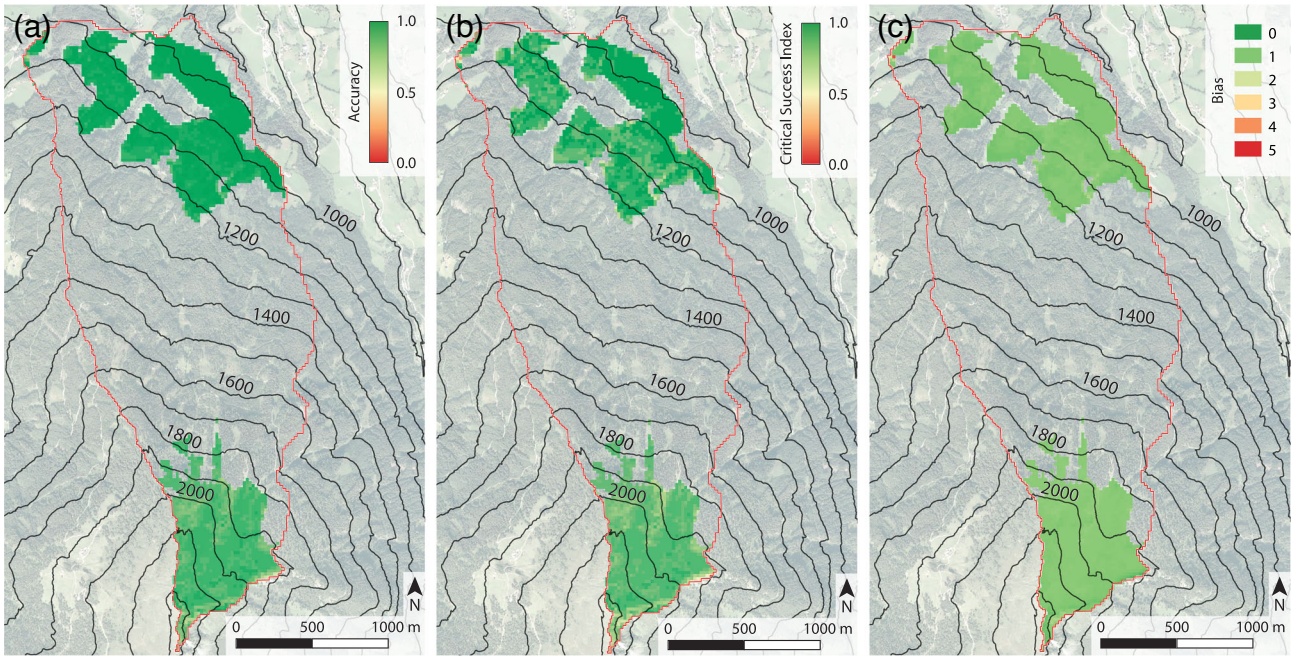

FIGURE 5 Validation results of the simulated snow cover extent and snow cover maps based on Sentinel-2 imagery. Metrics considered for the validation include the accuracy (ACC) (a), critical success index (CSI) (b) and bias (c)

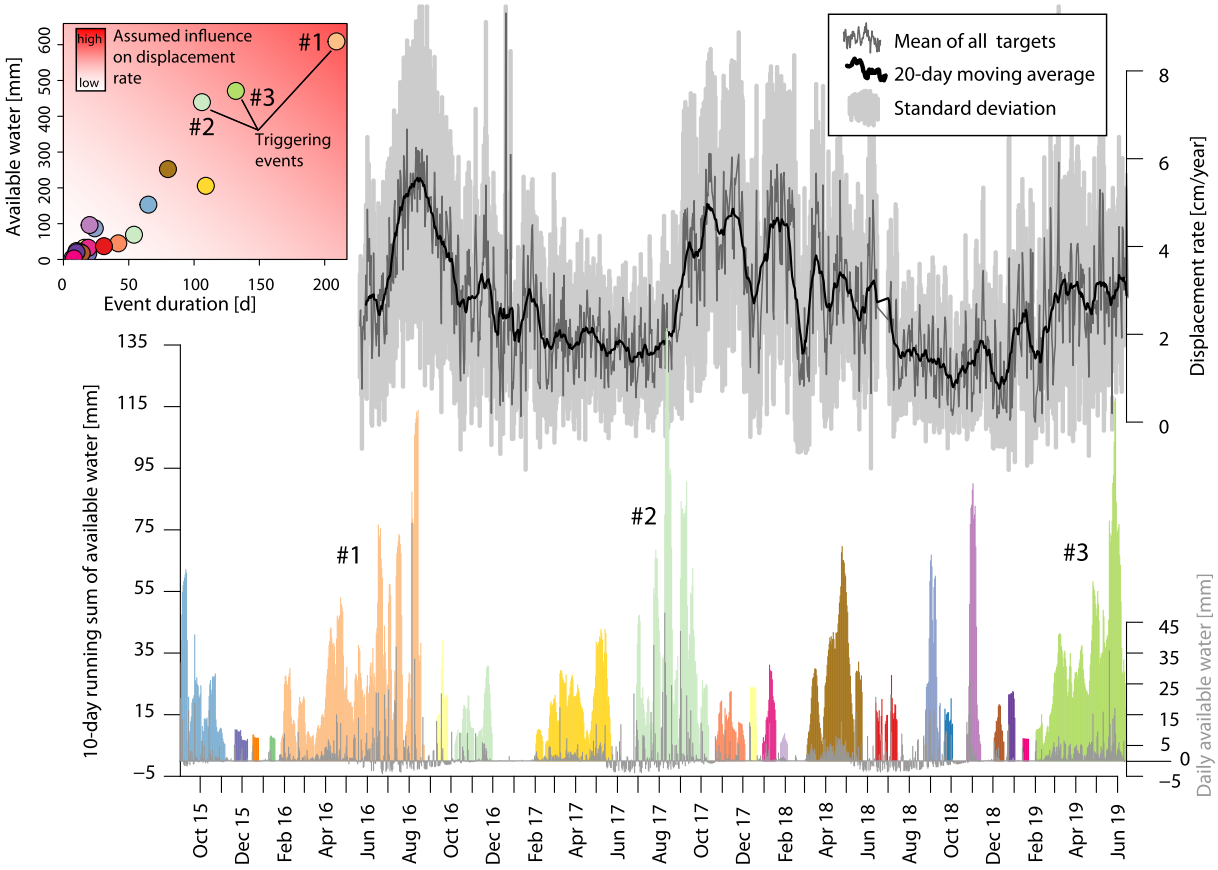

FIGURE 6 Extracted hydrometeorological events based on the 10-day running sum of spatially aggregated simulation results (coloured bars). The upper graph shows the mean movement rate of the 13 targets in the actively moving area (grey line) and a fitted spline (black line). The main acceleration phases in mid-2016, fall 2017 and spring 2018 follow prolonged hydrometeorological events (numbered). The plot at upper left shows the total available water versus the respective events' duration, with the three identified triggering events marked

closer to the active landslide body release higher amounts of water previously stored in the snow cover than the surrounding forested areas. Similar effects can be recognized in the annual mean distribution of available water (Figure 7d). A more balanced distribution pattern of simulated available water is observable during the rainfall-dominated event (event #2, Figure 7b).

TABLE 2 Characteristics of identified events associated with an increase in landslide displacement rate. Water values refer to the model domain. Annual average values are shown in the bottom row

Event	Start	End	Duration (d)	Available water (mm)	Rainfall (mm)	Snowmelt (mm)	Evapotranspiration (mm)	Displacement rate increase (cm/a)
#1	2016-01-27	2016-08-23	209	609	675	180	246	3.81
#2	2017-06-28	2017-10-12	106	439	584	15	160	2.87
#3	2019-02-02	2019-06-14	132	471	192	368	89	1.75
Average	2006-10-01	2018-09-30	365	643.5	764.7	236.6	357.7	–

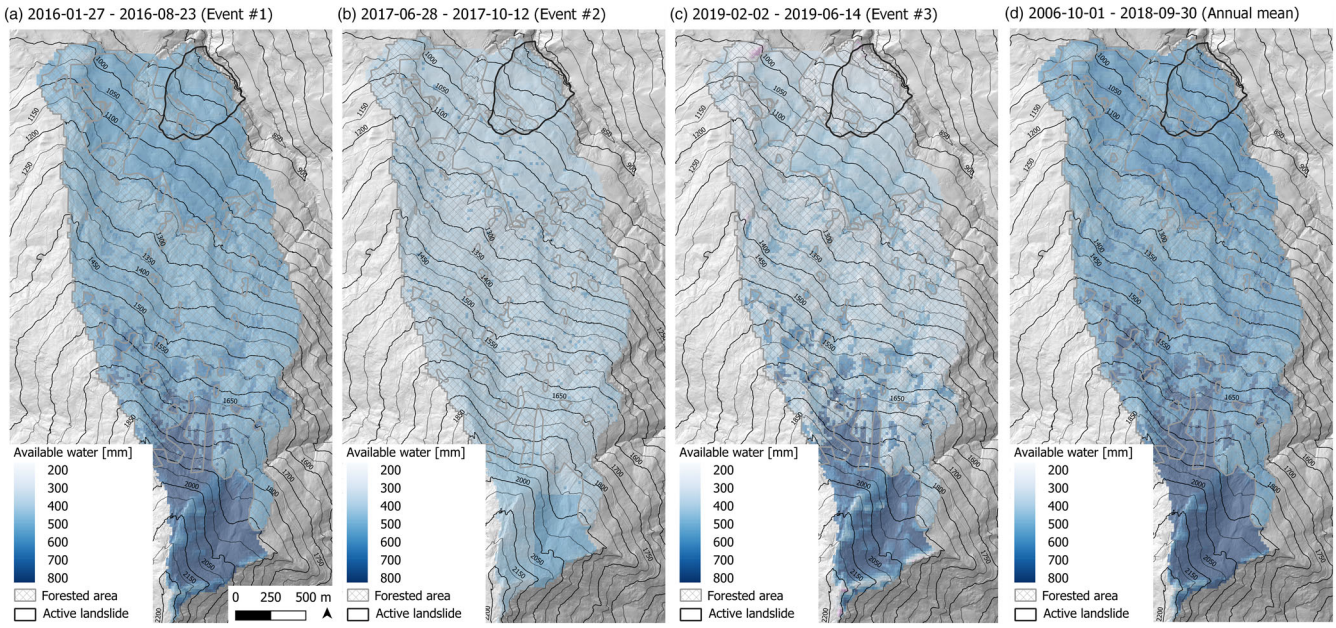

FIGURE 7 Available water sum and its spatial distribution for the identified triggering events from (a) 2016-01-27 to 2016-08-23 (event #1), (b) 2017-06-28 to 2017-10-12 (event #2), (c) 2019-02-02 to 2019-06-14 (event #3) and (d) annual mean values derived from the simulation results between 2006-10-01 and 2018-09-30

4.4 | Landslide response times

The water input time series derived for every raster cell in the model domain were cross-correlated with a time series of the mean landslide displacement rate in order to obtain spatial information of event-specific response times and correlation strengths. Response times were estimated by determining the earliest maximum of the respective cross-correlation function calculated for every raster cell of the spatio-temporal simulation results. In order to assess an appropriate cumulation window for calculating running sums of the water input time series, multiple cumulation windows ranging from 2 to 150 days were investigated regarding their correlation performance with the landslide movement time series. Therefore, cross-correlations between the mean landslide movement time series and various running sums of available water aggregated within 25 m elevation ranges were calculated for temporal subsets representing each triggering event.

Results show that the correlation strength generally enhances with increasing window size used for calculating the running sum of the available water time series (see Figure 8). A steep increase in correlation strength is observable until a window size of approximately 30 days (dashed black vertical lines in Figure 8), and thereafter the increase in correlation strength towards increasing window sizes is significantly lower. The 30-day window for calculating the running sum therefore produces good correlations while still respecting temporal changes in water input. As a consequence, the 30-day running sum of available water at every raster cell within the model domain was used as input for estimating its response time per prior identified event.

Derived response times for event #1 are in the range of approximately 20–60 days, where a general trend of increasing response time with increasing elevation and distance to the active landslide is obvious (Figures 9a and 10a). The landslide's response to the rainfall-dominated event #2, on the other hand, is spatially indifferent and can uniformly be approximated with a response time of 45 days (Figures 9b and 10b). The most recent event #3 triggering a pronounced acceleration of the landslide mainly due to snowmelt stands out concerning low response times in the order of −60 to 8 days (Figures 9c and 10c). Negative response times indicate raster cells where the landslide acceleration occurred prior to water becoming available for infiltration. Commonly, this is the case for snowmelt occurring later in spring at higher elevations when the landslide had already accelerated due to meltwater released earlier at lower elevations.

A heterogeneous response of landslide acceleration to variable water availability caused by different land cover types is apparent when investigating event #1 (Figure 9a). During this event the

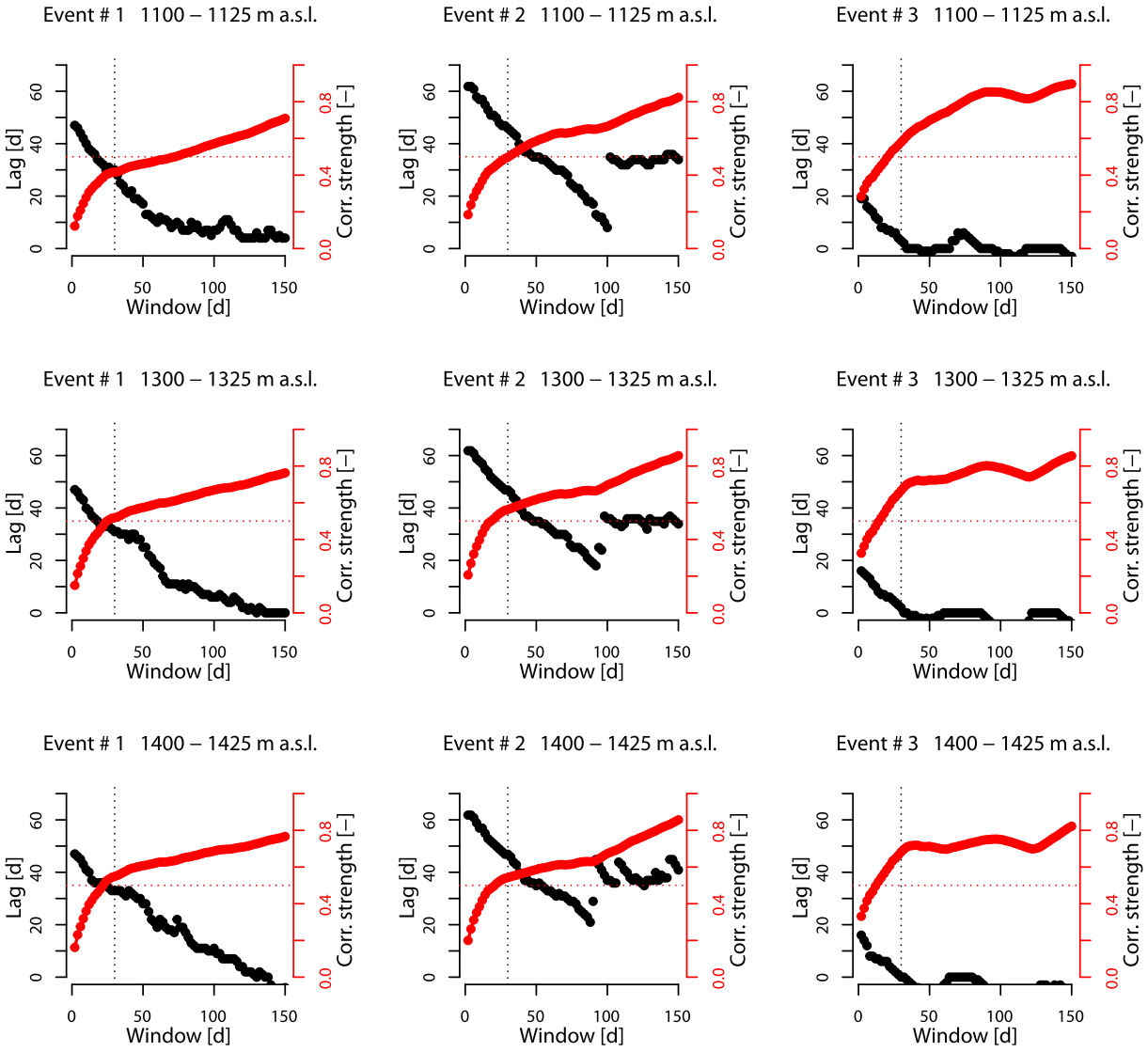

FIGURE 8 Cross-correlation results showing the influence of different window sizes for calculating the running sum of the water input time series at certain elevation bands. Red points indicate the maximum correlation strength between the water input and mean displacement rate time series at the respective time lag (black points). The dashed black line indicates the 30-day cumulation window where a distinct turn of the correlation strength curve occurs

response to water input in non-forested areas (approx. 24 days) arises 6 days earlier compared to the response in forested areas (approx. 30 days) while only considering areas below 1850 m a.s.l. (Figure 9a). The 1850 m a.s.l. contour line marks a distinct break between response times. During event #1 a sudden increase from 30 to 50 days of response time and during event #3 a sudden decrease from 0 to −52 days of response time towards higher elevations are evident (Figure 9a,c). Raster cells where no maximum within the cross-correlation function was found are more frequent at higher elevations further away from the active landslide part, indicating that water potentially infiltrating these areas may not contribute to the landslide's controlling aquifer.

Spatial differences of correlation strengths between the cross-correlated time series for each identified event are shown in Figure 9e–g. Good correlations between landslide movement and water input occur in forested areas above 1200 m a.s.l. for event #1. High correlation strength at raster cells below elevations of 1800 m a.s.l. are obvious for event #2. Best correlations for event #3 occur between 1300 and 1500 m a.s.l.

4.5 | Assessment of the landslide's hydrological catchment area

The results obtained from the area-wide cross-correlation offer essential information for delineating the landslide's effective hydrological catchment. Neglecting raster cells with response times less than 0 days results in a catchment extent ranging approximately from 750 to 1700 m a.s.l. (see Figure 9d). Within this range the highest values of the mean correlation strength of the three analysed events occur between 1250 and 1700 m a.s.l., indicating this range to be the most probable source of hydrometeorological water, causing pore pressure changes in the landslide's aquifer and leading to accelerated slope movements (Figure 9h).

To further delineate a laterally limited hydrological catchment, the upslope area of the lowest point in the active landslide was calculated. Additionally, the percentage contribution of every upslope raster cell to this initial raster cell was assessed (Tarboton, 1997). When only respecting raster cells potentially contributing more than 0.01% to the lowest point, the lateral extent of landslide hydrological

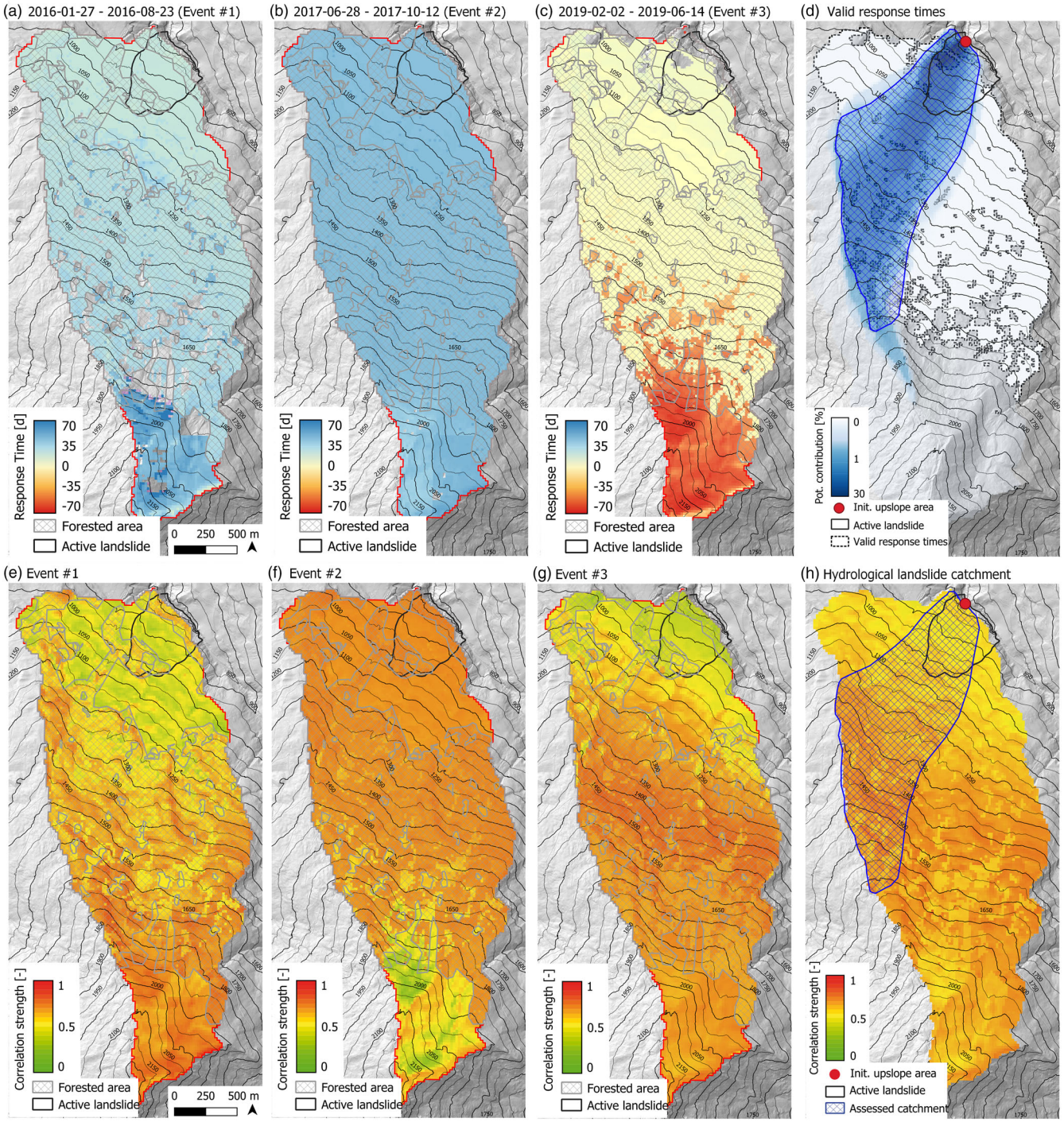

FIGURE 9 Spatial distribution of cross-correlation results (i.e., estimated response times and correlation) identifying a hydrological landslide catchment. (a,e) show results for event #1 (2016-01-27 to 2016-08-23), (b,f) for event #2 (2017-06-28 to 2017-10-12), and (c,g) for event #3 (2019-02-02 to 2019-06-14). (d) shows a potential source area by only allowing valid response times ($t_r > 0$ and <70 days) and raster cells potentially contributing with more than 0.01% to the lowest cell in the catchment and (h) shows the final assessed hydrological landslide catchment with mean correlation strengths indicating probable source of water forcing landslide movements

catchment was determined with a maximum lateral extent of 900 m. The delineated catchment is shown in Figure 9h, comprising a planimetric area of 1.43 km^2.

4.6 | The relation of landslide movement to water input

Temporally shifted dependencies arise when comparing the 30-day running sums of water input averaged within the delineated effective hydrological landslide catchment and landslide displacement rates (Figure 11a). The 30-day running sum of available water was identified to be a good proxy describing the time-delayed displacement rate. However, this presupposes knowledge of the event-specific time lag between the time series (see Section 4.4 and Figure 8). Only after shifting the landslide displacement rate time series backwards using the prior derived response times relations between displacement rate and water input become apparent. These can further be quantified by fitting logarithmic functions to the values occurring in both time series during individual hydrometeorological triggering events (Figure 11b,c).

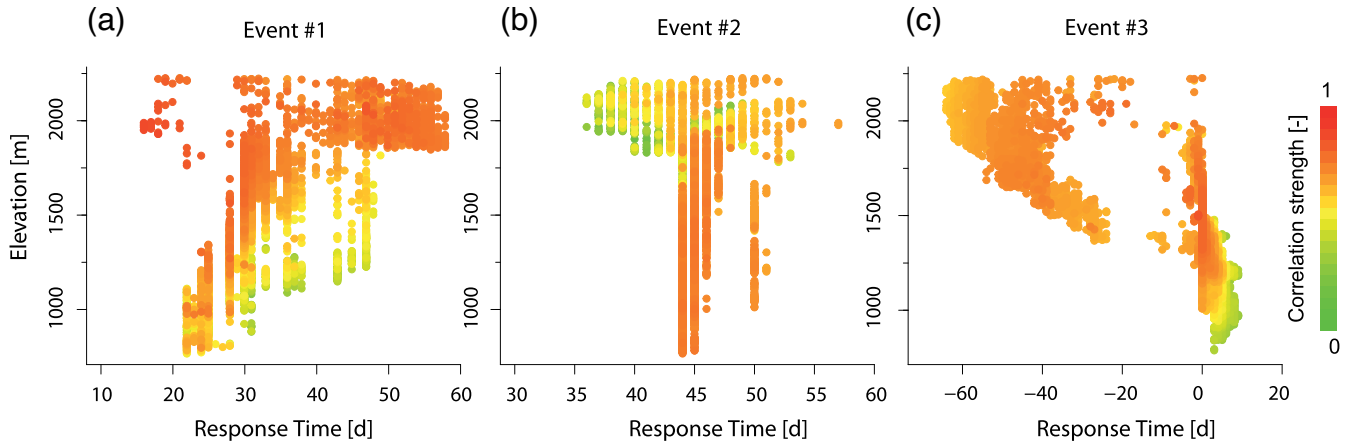

FIGURE 10 Estimated response times and elevation of respective raster cells estimated within the model domain and per landslide-triggering event: (a) 2016-01-27 to 2016-08-23 (event #1); (b) 2017-06-28 to 2017-10-12 (event #2); and (c) 2019-02-02 to 2019-06-14 (event #3). The colour represents the correlation strength of the cross-correlation between the hydrometeorological time series and the landslide displacement rate

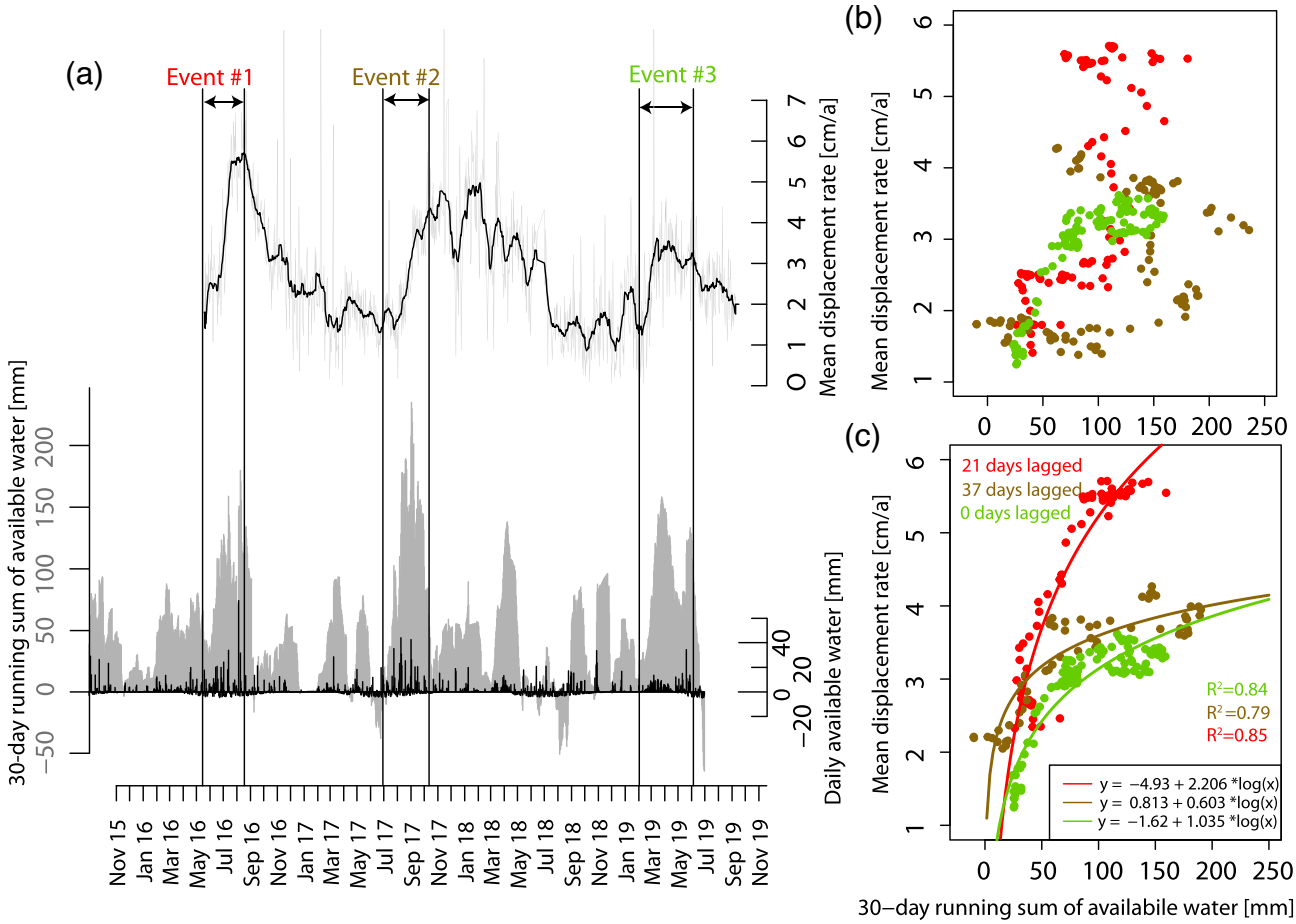

FIGURE 11 Relations between the modelled 30-day running sum of water availability within the delineated hydrological landslide catchment and measured mean landslide displacement rates: (a) comparison of respective time series; (b) relations between time series, ignoring apparent event-specific time lag; and (c) relations while respecting prior derived time lag, indicating logarithmic correlations between 30-day running sum of available water and landslide displacement rate

R^2 values of 0.85 for event #1, 0.79 for event #2 and 0.84 for event #3 indicate a good performance of fitted logarithmic models.

Respected time spans for model fitting conform to time spans of events retrieved for the effective hydrological landslide catchment. Major aberrations in event duration compared to the events derived in Section 4.3 arise from the different areas considered for aggregating the hydrological time series. Here we used the delineated effective hydrological landslide catchment, where in Section 4.3 the whole model domain was used.

All three models show an increase in displacement rate as a consequence of increasing water availability. The model's slope, indicating the increase in displacement rate, is generally steeper at lower values

of the 30-day running sum of water availability and flattens towards higher values. The models derived from events #2 and #3 are quite similar considering their coefficients. They indicate a steep increase in displacement rate from approximately 1.5 to 3.5 cm/a for event #2 and from 1 to 3 cm/a for event #3 as a result of an increase from 0 to 60 mm of cumulated water availability. A further increase in water availability from 60 to 200 mm only induces a small increase in displacement rate (in the order of approximately 0.5 cm/a).

The model derived for event #1 indicates a more sensitive response of landslide acceleration caused by water availability. Here the increase in displacement rate is more pronounced and ranges from 2 to 5.3 cm/a between 0 and 90 mm of cumulated water availability. From 90 mm towards higher water availability values the displacement rate increase flattens as in the models for events #2 and #3 but still reaches higher absolute displacement rate values.

The more sensitive response of landslide to water input during event #1 may be associated with different preconditions in terms of pre-event water. Within a 30-day time span 64 mm of water was available prior to event #1, but only 14 mm prior to event #3 and even negative amounts of −9 mm caused by distinct evapotranspiration prior to event #2 characterize the preconditions before the start of the succeeding triggering event (Figure 12).

5 | DISCUSSION

Applying the hydroclimatological model AMUNDSEN parametrized with meteorological data acquired at well-distributed surrounding weather stations allowed us to retrieve a well-validated spatio-temporal dataset of water availability in the study area around the Vögelsberg landslide. Validation of simulated snow depths, snow masses and spatial snow cover indicate a good model performance in simulating the evolution of the snowpack throughout the investigation period. Additionally, rainfall and evapotranspiration grids were used to retrieve the spatio-temporal pattern of water availability. The lack of on-site evapotranspiration reference data makes an evaluation of simulated evapotranspiration time series challenging. However, annual evaporation is in accordance with the long-term water balance of the Watten valley and similar to the regional estimate of Duethmann and Blöschl (2018).

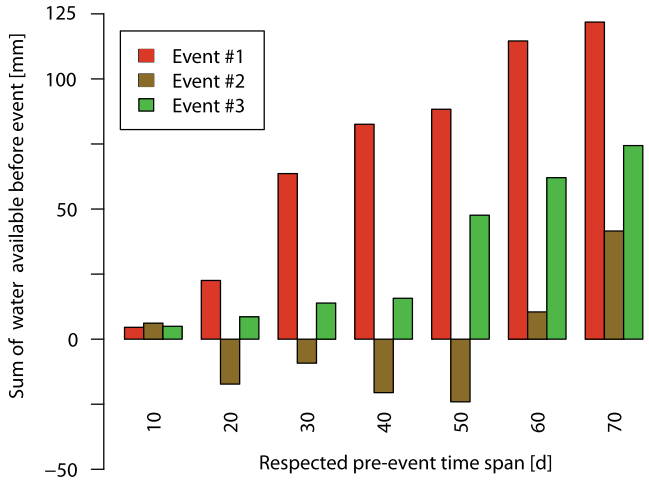

FIGURE 12 Water availability prior to the start of an identified landslide-accelerating hydrometeorological event respecting different pre-event time spans

Three outstanding landslide acceleration phases were observed within our study, each of them being triggered either by snowmelt, rainfall or both. Their temporal occurrence does not show a periodicity or seasonality. We quantified the hydrological drivers that control the individual response times and related them to the movement of the landslide. We also found distinct spatio-temporal patterns for each of the events. Derived landslide response times vary from 20 to 60 days for the combined rainfall- and snowmelt-induced event #1. We attribute the 40-day range of response times to the combined water input of snowmelt and rainfall, as well as to the long duration of the event (209 days). Snowmelt close to the active landslide is clearly related to shorter response times at the beginning of the event (in late winter/early spring), whereas snowmelt at higher elevations and rainfall in late spring and summer are related to longer response times.

The response time of 45 days for the rainfall-triggered event #2 is in conformity with Handwerger et al. (2013), who derived a response time of 40 days for similar sized and rainfall-triggered landslides by measuring the time lag between onset of seasonal precipitation and onset of seasonal acceleration. Landslide response to snowmelt, on the other hand, was observed to occur faster (0–8 days) in our case study. This circumstance suggests that observed snowmelt either occurs closer to the active landslide area or may infiltrate more efficiently than rainfall. This can be associated with the higher variability in duration and intensity of rainfall compared to snowmelt, which occurs more constantly over longer periods at seasons of less vegetation activity. Earman *et al.* (2006) estimated that 40–70% of groundwater recharge is snowmelt related in their study sites, although only 25–50% of average annual precipitation falls as snow. Similar observations of fast landslide response to snowmelt were made by Crosta et al. (2014), where landslide displacement recordings were compared with simulated snowmelt in a comparable landslide setting in the Italian Ferret valley.

Excluding areas where water availability occurs after landslide acceleration (response time < 0) allowed us to assess the elevation ranges, where hydrometeorological water can infiltrate and cause distinct pore pressure changes in the landslide aquifer. Combining this information with results obtained from a flow–accumulation algorithm allowed us to delineate a catchment that strongly relies on the pronounced spatio-temporal variability of snowmelt and may not fully represent the landslide-affecting hydrological area during uniform rainfall events. Nevertheless, highest correlation strengths between cross-correlated hydrological and displacement rate time series occur within the estimated landslide-affecting catchment, and strengthen the reliability of its boundaries. Furthermore, the occurrence of high correlation strengths between 1200 and 1700 m a.s.l. allows a spatial weighting of where the simulated available water is more likely to contribute to landslide acceleration. Water balance interventions such as the prevention of infiltration or strengthening the evapotranspiration in this identified area are further assumed to have the greatest influence on the reduction of groundwater recharge, potentially inducing a reduced amplitude of the landslide displacement rate curve.

Despite the distinct differences in the hydrological landslide drivers, we can conclude from event #3 that infiltrating snowmelt on

areas close to the landslide can cause an immediate acceleration of its movement. On the other hand, we see that prolonged rainfall causes a balanced and more delayed landslide response holding true for event #2 and partially for event #1, where we cannot exclude the influence of snowmelt at high elevations. This may not be the main driving forces for landslide movement during the investigated events, but can still contribute to the precondition. Although we are aware that the limited number of investigated events may prevent investigating a long-term correlation of hydrological drivers and the landslide's response (e.g., rainfall thresholds for the initiation of accelerated movements), some coherent patterns are observable. Moreover, we see that observed landslide acceleration phases are driven by various hydrological drivers. Furthermore, this leads to individual event response times and displacement rate–water input relationships with a strong connection to the water input prior to the hydrometeorological event.

We found logarithmic relationships between the displacement rate and water input for each of the events, but their difference – i.e., the event-to-event variability – suggests that the response of the landslide varies, depending on hydrological preconditions and system states. Nevertheless, hydrogeological conditions in nature are complex and require further on-site investigations (e.g., long-term measurements of groundwater level, geological mapping, estimations of groundwater recharge elevation) to validate established assumptions and to create a more consistent groundwater model. When parametrizing numerical groundwater models, additional knowledge of surface runoff has to be acquired to complete necessary variables for groundwater recharge estimation.

Although the quality of displacement rates and simulated water availability time series were well assessed (Sections 4.2 and 4.1), quantifying the uncertainty of the derived response times remains challenging. Temporal aggregation of the highly resolved displacement time series is necessary to retrieve valuable information about the landslide displacement rates within the observation period, but may also be consistent with a loss of quality in terms of the temporal prediction of the respective start of acceleration and deceleration phases. An additional influence on response times is attributed to the temporal accuracy of simulated water availability time series. For simulated snow depth times series we see that snowmelt is predicted earlier by the hydroclimatological model compared to the observed snowmelt reaching a maximum shift of 9 days at the lowest validation weather station during winter 2019. Accounting for this offset would cause a small shift of respective response times towards lower values in the range of a maximum of 9 days.

Limitations due to data availability are apparent within our study. In particular, missing displacement records prior to the beginning of the first acceleration phase may cause biased response times. Recently collected groundwater-level measurements were not yet available for this study, but very likely may strengthen our prior assumption that changes in landslide displacement rate are driven by pore-water pressure changes.

6 | CONCLUSIONS

Applying the AMUNDSEN hydroclimatological model allowed us to accurately assess hydrological drivers (i.e., rainfall, snowmelt), which are important for groundwater recharge and hence control the pore-water pressure and landslide movement. Point validation of simulated snow depths and snow masses as well as a spatial validation of the snow cover evolution throughout the winter months using satellite-supported reference data indicate a good model performance. Simulated rainfall, snowmelt and evapotranspiration were further used to derive time series of available water for every raster cell of the landslide catchment. A rule-based segmentation approach applied on time series of available water was used to extract hydrometeorological events, whose magnitude and duration are consistent with the subsequent magnitude of landslide displacement rate increase.

Three major phases of increased landslide displacement rate can be associated with three outstanding hydrometeorological events lasting for 106–209 days but implicating between 68% and 95% of water that is normally received during a whole year. Potential landslide response to the triggering event was derived for every raster cell and event by cross-correlating a 30-day running sum of water input time series with a mean displacement rate time series. Landslide acceleration in response to snowmelt nearby occurs in a couple of days (0–8), whereas the response to rainfall takes 45 days. Reasonable response times were used to delineate the landslide's effective hydrological catchment.

Spatially aggregated hydrological time series within this catchment boundaries were used to derive statistical models for the three events describing the behaviour of landslide displacement rate in response to water input. Fitted logarithmic models seem to describe this relation quite well, when considering respective time lag between the two time series. For two events where no significant amounts of water were available prior to the event, we observed a logarithmic increase of displacement rate until a steady level of 3–4 cm/a. No further acceleration in response of water input can be observed after reaching this level. For an event with considerable amounts of water already being feed to the slope's hydrological system beforehand, the displacement rate increase is observed to be more sensitive until a quasi-steady level of 5.5 cm/a is reached.

The present study shows how hydrological landslide drivers can be accurately assessed in both high temporal and spatial resolution and how this information, combined with continuous landslide displacement rate records, can be used to draw conclusions about hydrological processes causing increased landslide displacement rates. Combining these results with further on-site hydrogeological investigations and monitoring may help in validating, clarifying, strengthening and deepening the understanding of the involved processes.

ACKNOWLEDGEMENTS

The present study was conducted within the OPERANDUM project. This project has received funding from the European Union's Horizon 2020 research and innovation programme under grant agreement No. 776848. We thank the Federal state of Tyrol, Division of Geoinformation for providing ATTS measurements, the Austrian Research Centre for Forests for providing hydrological data and the Austrian Service for Torrent and Avalanche Control for the exchange of valuable information.

CONFLICT OF INTEREST

The authors declare no conflict of interest.

DATA AVAILABILITY STATEMENT

The AMUNDSEN hydroclimatological model data that support the findings of this study will be openly available on the PANGAEA® data publishing platform (publication ongoing).

ORCID

Jan Pfeiffer https://orcid.org/0000-0001-5352-6047
Thomas Zieher https://orcid.org/0000-0003-2985-5689
Jan Schmieder https://orcid.org/0000-0003-1521-3984
Martin Rutzinger https://orcid.org/0000-0001-6628-4681
Ulrich Strasser https://orcid.org/0000-0003-4776-2822

REFERENCES

Agliardi, F., Crosta, G.B. & Frattini, P. (2012) Slow rock-slope deformation. In: Clague, J.J. & Stead, D. (Eds.) *Landslides: Types, mechanisms and modeling*. Cambridge University Press: Cambridge, UK, pp. 207–221.

Ambrosi, C. & Crosta, G.B. (2006) Large sackung along major tectonic features in the Central Italian Alps. *Engineering Geology*, 83(1), 183–200. Available from: http://www.sciencedirect.com/science/article/pii/S0013795205002292

Bievre, G., Joseph, A. & Bertrand, C. (2018) Preferential water infiltration path in a slow-moving clayey earthslide evidenced by cross-correlation of hydrometeorological time series (Charlaix landslide, French Western Alps). *Geofluids*, 2018, article ID 9593267.

Bonzanigo, L., Eberhardt, E. & Loew, S. (2007) Long-term investigation of a deep-seated creeping landslide in crystalline rock. Part I. Geological and hydromechanical factors controlling the Campo Vallemaggia landslide. *Canadian Geotechnical Journal*, 44(10), 1157–1180. Available from: https://doi.org/10.1139/T07-043

Bovis, M.J. & Evans, S.G. (1996) Extensive deformations of rock slopes in southern coast mountains, southwest British Columbia, Canada. *Engineering Geology*, 44(1), 163–182. Available from: https://doi.org/10.1016/S0013-7952(96)00068-3

Brückl, E., Brunner, F.K., Lang, E., Mertl, S., Müller, M. & Stary, U. (2013) The Gradenbach Observatory monitoring deep-seated gravitational slope deformation by geodetic, hydrological, and seismological methods. *Landslides*, 10(6), 815–829.

Caine, N. (1980) The rainfall intensity–duration control of shallow landslides and debris flows. *Geografiska Annaler: Series A, Physical Geography*, 62(1–2), 23–27. Available from: https://doi.org/10.1080/04353676.1980.11879996

Carlà, T., Intrieri, E., Di Traglia, F., Nolesini, T., Gigli, G. & Casagli, N. (2017) Guidelines on the use of inverse velocity method as a tool for setting alarm thresholds and forecasting landslides and structure collapses. *Landslides*, 14(2), 517–534.

Coe, J.A. (2012) Regional moisture balance control of landslide motion: Implications for landslide forecasting in a changing climate. *Geology*, 40(4), 323–326. Available from: https://doi.org/10.1130/G32897.1

Crosta, G.B., Frattini, P. & Agliardi, F. (2013) Deep seated gravitational slope deformations in the European Alps. *Tectonophysics*, 605, 13–33. Available from: http://www.sciencedirect.com/science/article/pii/S0040195113002837

Crosta, G.B., Di Prisco, C., Frattini, P., Frigerio, G., Castellanza, R. & Agliardi, F. (2014) Chasing a complete understanding of the triggering mechanisms of a large rapidly evolving rockslide. *Landslides*, 11(5), 747–764.

de Palézieux, L. & Loew, S. (2019) Long-term transient groundwater pressure and deep infiltration in Alpine mountain slopes (Poschiavo Valley, Switzerland). *Hydrogeology Journal*, 27(8), 2817–2834.

Duethmann, D. & Blöschl, G. (2018) Why has catchment evaporation increased in the past 40 years? A data-based study in Austria. *Hydrology and Earth System Sciences*, 22(10), 5143–5158. Available from: https://hess.copernicus.org/articles/22/5143/2018/

Earman, S., Campbell, A.R., Phillips, F.M. & Newman, B.D. (2006) Isotopic exchange between snow and atmospheric water vapor: Estimation of the snowmelt component of groundwater recharge in the southwestern United States. *Journal of Geophysical Research: Atmospheres*, 111(D9), D09302. Available from: https://agupubs.onlinelibrary.wiley.com/doi/abs/10.1029/2005JD006470

Eberhardt, E. Bonzanigo, L., & Loew, S. (2007) Long-term investigation of a deep-seated creeping landslide in crystalline rock. Part II. Mitigation measures and numerical modelling of deep drainage at Campo Vallemaggia. *Canadian Geotechnical Journal*, 44(10), 1181–1199. Available from: https://doi.org/10.1139/T07-044

Engl, D. (2018) Aktueller Kenntnisstand Hangbewegung Vögelsberg, Gemeinde Wattens, Forsttechnischer Dienst für Wildbach- und Lawinenverbauung. Innsbruck.

Gascoin, S., Grizonnet, M., Bouchet, M., Salgues, G. & Hagolle, O. (2019) Theia Snow collection: High-resolution operational snow cover maps from Sentinel-2 and Landsat-8 data. *Earth System Science Data*, 11(2), 493–514. Available from: https://www.earth-syst-sci-data.net/11/493/2019/

Guzzetti, F., Peruccacci, S., Rossi, M. & Stark, C.P. (2008) The rainfall intensity–duration control of shallow landslides and debris flows: An update. *Landslides*, 5(1), 3–17.

Handwerger, A.L., Roering, J.J. & Schmidt, D.A. (2013) Controls on the seasonal deformation of slow-moving landslides. *Earth and Planetary Science Letters*, 377–378, 239–247. Available from: http://www.sciencedirect.com/science/article/pii/S0012821X13003701

Hanzer, F., Helfricht, K., Marke, T. & Strasser, U. (2016) Multilevel spatio-temporal validation of snow/ice mass balance and runoff modeling in glacierized catchments. *The Cryosphere*, 10(4), 1859–1881. Available from: http://doi.org/10.5194/tc-10-1859-2016

Iverson, R.M. & Major, J.J. (1987) Rainfall, ground-water flow, and seasonal movement at Minor Creek landslide, northwestern California: Physical interpretation of empirical relations. *GSA Bulletin*, 99(4), 579–594. Available from: https://doi.org/10.1130/0016-7606(1987)99<579:RGFASM>2.0.CO;2

Kling, H., Fuchs, M. & Paulin, M. (2012) Runoff conditions in the upper Danube basin under an ensemble of climate change scenarios. *Journal of Hydrology*, 424–425, 264–277. Available from: https://doi.org/10.1016/j.jhydrol.2012.01.011

Lacroix, P., Handwerger, A.L. & Bièvre, G. (2020) Life and death of slow-moving landslides. *Nature Reviews Earth and Environment*, 1(8), 404–419.

Lollino, G., Arattano, M. & Cuccureddu, M. (2002) The use of the automatic inclinometric system for landslide early warning: The case of Cabella Ligure (north-western Italy). *Physics and Chemistry of the Earth, Parts A/B/C*, 27(36), 1545–1550. Available from: http://www.sciencedirect.com/science/article/pii/S1474706502001754

Lollino, G., Arattano, M., Allasia, P. & Giordan, D. (2006) Time response of a landslide to meteorological events. *Natural Hazards and Earth System Sciences*, 6(2), 179–184. Available from: https://nhess.copernicus.org/articles/6/179/2006/

Macfarlane, D.F. (2009) Observations and predictions of the behaviour of large, slow-moving landslides in schist, Clyde Dam reservoir, New Zealand. *Engineering Geology*, 109(1), 5–15. Available from: http://www.sciencedirect.com/science/article/pii/S0013795209000325

Marke, T., Strasser, U., Hanzer, F., Stötter, J., Wilcke, R.A.I. & Gobiet, A. (2015) Scenarios of future snow conditions in Styria (Austrian Alps). *Journal of Hydrometeorology*, 16(1), 261–277. Available from: https://doi.org/10.1175/JHM-D-14-0035.1

Meißl, G., Zieher, T. & Geitner, C. (2020) Runoff response to rainfall events considering initial soil moisture analysis of 9-year records in a small alpine catchment (Brixenbach Valley, Tyrol, Austria). *Journal of Hydrology: Regional Studies*, 30, 100711. Available from: http://www.sciencedirect.com/science/article/pii/S2214581820301853

Osawa, H., Matsushi, Y., Matsuura, S., Okamoto, T., Shibasaki, T. & Hirashima, H. (2018) Seasonal transition of hydrological processes in a slow-moving landslide in a snowy region. *Hydrological Processes*, 32(17), 2695–2707. Available from: https://onlinelibrary.wiley.com/doi/abs/10.1002/hyp.13212

Ostermann, M. & Sanders, D. (2017) The Benner Pass rock avalanche cluster suggests a close relation between long-term slope deformation

(DSGSDs and translational rock slides) and catastrophic failure. *Geomorphology*, 289, 44–59. Available from: http://www.sciencedirect.com/science/article/pii/S0169555X16312296

Pellicciotti, F., Brock, B., Strasser, U., Burlando, P., Funk, M. & Corripio, J. (2005) An enhanced temperature-index glacier melt model including the shortwave radiation balance: Development and testing for Haut Glacier Arolla, Switzerland. *Journal of Glaciology*, 51(175), 573–587. Available from: https://doi.org/10.3189/172756505781829124

Pfeiffer, J., Zieher, T., Bremer, M., Wichmann, V. & Rutzinger, M. (2018) Derivation of three-dimensional displacement vectors from multi-temporal long-range terrestrial laser scanning at the Reissenschuh landslide (Tyrol, Austria). *Remote Sensing*, 10(11), 1688. Available from: http://doi.org/10.3390/rs10111688

R Core Team. (2020) R: A language and environment for statistical computing. R Foundation for Statistical Computing, Vienna, Austria. Available from: https://www.R-project.org/

Rockenschaub, M., Kolenprat, B. & Nowotny, A. (2003) Innsbrucker quarzphyllitkomplex, tarntaler mesozoikum, patscherkofelkristallin. Arbeitstagung 2003, Blatt 148. Geologische Bundesanstalt, Brenner; pp. 41–58.

Ruangpan, L., Vojinovic, Z., Di Sabatino, S., Leo, L.S., Capobianco, V., Oen, A.M.P., McClain, M.E. & Lopez-Gunn, E. (2020) Nature-based solutions for hydro-meteorological risk reduction: A state-of-the-art review of the research area. *Natural Hazards and Earth System Sciences*, 20(1), 243–270. Available from: https://nhess.copernicus.org/articles/20/243/2020/

Strasser, U. (2008) Modelling of the mountain snow cover in the Berchtesgaden National Park. *Forschungsberichte des Nationalpark Berchtesgaden*, 55, 1–184.

Strasser, U., Bernhardt, M., Weber, M., Liston, G.E. & Mauser, W. (2008) Is snow sublimation important in the alpine water balance? *The Cryosphere*, 2(1), 53–66. Available from: https://www.the-cryosphere.net/2/53/2008/

Tarboton, D.G. (1997) A new method for the determination of flow directions and upslope areas in grid digital elevation models. *Water Resources Research*, 33(2), 309–319. Available from: https://agupubs.onlinelibrary.wiley.com/doi/abs/10.1029/96WR03137

Terzaghi, K. (1950) Mechanism of Landslides. In *Application of Geology to Engineering Practice*. Geological Society of America: Boulder, CO. Available from: https://doi.org/10.1130/Berkey.1950.83

Vallet, A., Bertrand, C., Fabbri, O. & Mudry, J. (2015) An efficient workflow to accurately compute groundwater recharge for the study of rainfall-triggered deep-seated landslides, application to the Schilienne unstable slope (Western Alps). *Hydrology and Earth System Sciences*, 19(1), 427–449. Available from: https://hess.copernicus.org/articles/19/427/2015/

Van Genuchten, P.B. & Van Asch, T.W.J. (1988) Factors controlling the movement of a landslide in varved clays near La Mure (French Alps). *Bulletin de la Société Géologique de France*, IV(3), 461–469. Available from: https://doi.org/10.2113/gssgfbull.IV.3.461

Varnes, D.J., Radbruch-Hall, D.H., Varnes, K.L., Smith, W.K. & Savage, W.Z. (1990) Measurement of ridge-spreading movements (sackungen) at Bald Eagle Mountain, Lake County, Colorado, 1975–1989, US Geological Survey, Department of the Interior: Washington, DC. Available from: http://pubs.er.usgs.gov/publication/ofr00205

Zangerl, C., Eberhardt, E. & Perzlmaier, S. (2010) Kinematic behaviour and velocity characteristics of a complex deep-seated crystalline rockslide system in relation to its interaction with a dam reservoir. *Engineering Geology*, 112(1), 53–67. Available from: http://www.sciencedirect.com/science/article/pii/S0013795210000025

Zappa, M. (2008) Objective quantitative spatial verification of distributed snow cover simulations: An experiment for the whole of Switzerland. *Hydrological Sciences Journal*, 53(1), 179–191. Available from: https://doi.org/10.1623/hysj.53.1.179

Zieher, T., Bremer, M., Rutzinger, M., Pfeiffer, J., Fritzmann, P. & Wichmann, V. (2019) Assessment of landslide-induced displacement and deformation of above-ground objects using UAV-borne and airborne laser scanning data. *ISPRS Annals of Photogrammetry, Remote Sensing and Spatial Information Sciences*, IV-2/W5, 461–467. Available from: https://www.isprs-ann-photogramm-remote-sens-spatial-inf-sci.net/IV-2-W5/461/2019/

How to cite this article: Pfeiffer, J., Zieher, T., Schmieder, J., Rutzinger, M. and Strasser, U. (2021) Spatio-temporal assessment of the hydrological drivers of an active deep-seated gravitational slope deformation: The Vögelsberg landslide in Tyrol (Austria). *Earth Surface Processes and Landforms*, 1–17. Available from: https://doi.org/10.1002/esp.5129